On the formation of the porous structure in nanostructured a-Si coatings deposited by dc magnetron sputtering at oblique angles

V Godinho[1], **P Moskovkin**[2], **R Álvarez**[1], **J Caballero-Hernández**[1],
R Schierholz[1], **B Bera**[2], **J Demarche**[2], **A Palmero**[1], **A Fernández**[1] and
S Lucas[2]

[1] Instituto de Ciencia de Materiales de Sevilla (CSIC-US), Seville, Spain
[2] Research Centre for the Physics of Matter and Radiation (PMR-LARN), University of Namur (FUNDP), Namur, Belgium

E-mail: godinho@icmse.csic.es

Abstract

The formation of the porous structure in dc magnetron sputtered amorphous silicon thin films at low temperatures is studied when using helium and/or argon as the processing gas. In each case, a-Si thin films were simultaneously grown at two different locations in the reactor which led to the assembly of different porous structures. The set of four fabricated samples has been analyzed at the microstructural level to elucidate the characteristics of the porous structure under the different deposition conditions. With the help of a growth model, we conclude that the chemical nature of the sputter gas not only affects the sputtering mechanism of Si atoms from the target and their subsequent transport in the gaseous/plasma phase towards the film, but also the pore formation mechanism and dynamics. When Ar is used, pores emerge as a direct result of the shadowing processes of Si atoms, in agreement with Thornton's structure zone model. The introduction of He produces, in addition to the shadowing effects, a new process where a degree of mobility results in the coarsening of small pores. Our results also highlight the influence of the composition of sputtering gas and tilt angles (for oblique angle deposition) on the formation of open and/or occluded porosity.

Keywords: porous silicon, oblique angle deposition, growth model, Monte Carlo simulation, magnetron sputtering, porosity formation, nanostructure

(Some figures may appear in colour only in the online journal)

1. Introduction

Porous silicon is nowadays one of the most actively researched materials with applications in sensors, photonic devices, microelectronics or solar energy conversion, among others (see for instance [1–4] and references therein). Although this material has been widely and deeply studied in the past decades, there are numerous fundamental issues still under research regarding the control of the silicon film structure in small scales [5]. Traditionally, porous silicon is prepared by electrochemical anodization of crystalline silicon in hydrofluoric acid. By changing the electrolyte concentration and the applied current, different open porous structures can be obtained [6, 7]. In a recent publication, we presented a novel, bottom-up methodology for producing porous silicon coatings with closed porosity based on the magnetron sputtering deposition technique [8]. There, we showed that the use of He as the processing gas gives rise to singular microstructures with occluded porosity, aligned along a certain preferential

direction. These films present many advantages for integration in functional devices, as aging effects and material degradation associated with the filling of the pores with environmental gases (e.g., water) are drastically reduced. The novelty of this new methodology in the context of the fabrication of porous silicon structures by magnetron sputtering is related to the formation and control of closed porosity with a tailored refractive index [8]. The paper also presented the influence of changing deposition parameters like discharge power, deposition angle or gas composition on the final microstructure and properties of the films [8].

From this work [8], and other previous investigations in our laboratory [9–11], it was concluded that the chemical nature of the processing gas might be critical for the development of a certain closed porous structure. Thus, in the present paper our aim is to investigate this issue by performing selected experiments with different processing gases, Ar and He, and analyzing the occluded porosity of silicon films aided by a growth model using oblique angle deposition geometry (OAD). The conditions have been selected by choosing (i) helium and/or argon as the processing gas, (ii) two different positions in the reactor and (iii) a low dc power (150 W). The aim is to obtain conclusions on the basis of these four selected samples and conditions on the formation mechanism of the porous a-Si thin films. Remarkably, many studies in the literature, using atomistic growth models and experiments, have analyzed the influence on the nanostructure of deposition conditions such as the angular incidence of vapor particles onto the film [12], the film temperature during growth [13] or the role of potential barriers [14]. To our knowledge, the influence of the processing gas on the film nanostructure was not yet clear. As we will show in the present paper, our results indicate that the chemical nature of the sputter gas not only affects the sputter mechanism and the collisional processes in the gaseous/plasma phase, but also pore formation and dynamics within the material, and thus the film microstructure. In addition, pore formation by He ion implantation of deposited metal thin films has been studied thanks to its importance in nuclear technology [15–18]. Indeed, to re-create the conditions of reactors and cold plasma in contact with the reactor walls, He has been artificially introduced into materials using well-known plasma-assisted techniques, such as magnetron sputtering of different metals in He/Ar mixtures [15–18]. In these studies [15–20], the authors claim that the highly ionized He ions bombarding the target are backscattered or attracted by the negative substrate bias and implanted into the film. Furthermore, Jäger [21] and colleagues found that He bubbles are formed inside the material thanks to its low solubility, which promotes point defect mobility and the merging of voids, phenomena that are essentially different when Ar is employed. Several models have been proposed to describe the behavior of implanted He atoms in metals [20, 22, 23], although, to our knowledge, no fundamental studies have been carried out in the literature to discern whether mobility processes induced by embedded He affect the growth and nanostructural development of as-deposited thin films.

In summary, in this work we shed light on the microstructural evolution of magnetron sputtered a-Si coatings, comparing experimental results (by transmission electron microscopy (TEM)) with computer simulations in carefully chosen conditions. For that, and as a first approach, we make use of a ballistic aggregation Monte Carlo (MC) simulation to understand the influence of atomistic processes on the formation of the film nanostructure during growth when He and/ or Ar are employed. These types of models are particularly useful in situations where geometric mechanisms govern the formation of the nanostructure, such as when the film growth takes place at low temperatures (i.e. in zone I of Thornton's structure zone model [24–27]). It should also be emphasized here that under the selected low dc power conditions, the low plasma potential (about ~5 V) will cause positive ions to impinge on the growing film with energies below any surface mobility threshold [28]. In this regard, the well-known and widely-employed NASCAM software [29, 30] has been used to analyze film growth. This widely employed computer code has already helped explain numerous issues regarding the kinetic energy of the vapor particles and the bond structure and chemical nature of the films. Future work will include the introduction of the effect of high plasma potential under RF power and helium mobility.

2. Experimental details

2.1. Preparation of the coatings

To elucidate the growth mechanism and the atomistic processes responsible for the formation of the porous network in the films, a set of experimental conditions were carefully chosen. A dc electromagnetic field with a power of 150 W was employed to maintain the magnetron sputtering plasma. This was done to achieve low plasma potentials during deposition (~5 V), which causes positive ions to impinge on the film with energies below any surface mobility threshold.

The coatings were deposited at an oblique angle, with the magnetron head tilted 30° with respect to the substrate holder orientation. To investigate the influence of the deposition geometry on the microstructure of the coatings, two different films were grown; both located on a plane at 5 cm vertical distance from the magnetron head. As shown in figure 1, one was placed 2 cm (zone 1 (Z1)) and the other 6 cm (zone 2 (Z2)) from the vertical location of the magnetron head above the substrate holder.

The target was made of pure Si (Kurt J Lesker 99.999% pure, 2′ diameter). The base pressure in the chamber before deposition was 5×10^{-5} Pa. The influence of the deposition gas on porosity was investigated using both (i) a mixture of He and Ar as sputter gas with a partial pressure of 1.7 Pa of He and 0.8 Pa of Ar gas (the Ar partial pressure was set to the minimum value to sustain the discharge) (ii) and pure Ar at a pressure of 1.4 Pa. The coatings were mainly deposited on polished silicon (100) while carbon glass was used only for the Rutherford backscattering spectrometry (RBS) analysis to get a better separation of the Si signal from the coating and
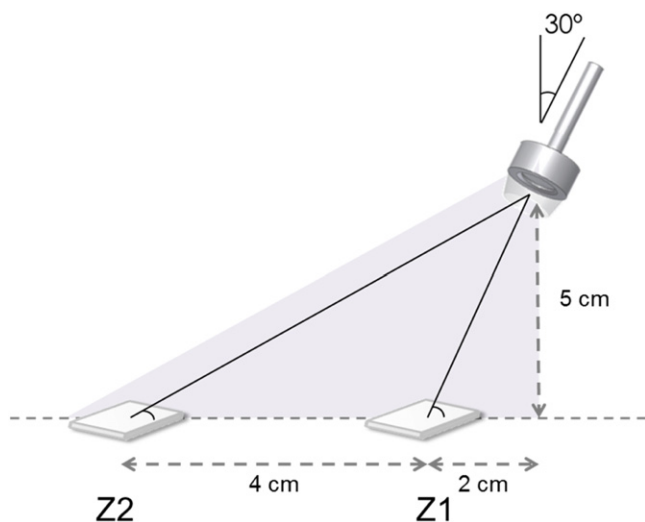
Figure 1. Experimental setup.

substrate. According to our previously reported results [8], we have been able to grow the same a-Si porous layers on crystalline (i.e. Si(100)) and amorphous (i.e. Teflon) substrates.

The low temperatures achieved during deposition (below 130 °C in all studied cases), imply a value of the homologous temperature of about, $T_s/T_m \sim 0.2$, where T_s is the substrate temperature and T_m the melting point of silicon. Therefore, the growth falls within zone I of Thornton's structure zone model, where thermally activated processes possess limited efficiency in comparison with geometrical (shadowing) effects.

2.2. Characterization of the coatings

The microstructure of the coatings, pore size and distribution were investigated by TEM using a Philips CM200 and an FEI Tecnai F30 microscope operated at 200 and 300 kV, respectively (LANE laboratory at the ICMS). Cross-sectional specimens were prepared in the conventional way by mechanical polishing, followed by Ar$^+$ ion milling to achieve electron transparency of the coatings deposited on Si substrates. Before the analysis, the samples were cleaned inside the TEM holder with Ar/O$_2$ plasma. The pore distribution was evaluated from the TEM micrographs as shown in figure 2. The images were processed with image analysis software to identify the pores as well-defined dark contrast areas (see figures 2(b) and (c)) which were then analyzed with the 'analyze particle function' of the ImageJ software [31]. To compare with the simulation results, the effective pore diameter was calculated by software from the measured pore area considering round pores. Energy filtered TEM (EFTEM) images were extracted from EFTEM spectrum-image data recorded with a 4 eV slit width with 2 eV steps using the Tecnai F30 microscope equipped with a GIF Quantum 963 energy filter device.

Scanning electron microscopy (SEM) analysis was carried out in cross-sectional views using a Hitachi S4800 SEM-FEG microscope.

The composition of the films was evaluated by RBS using a 2.5 MeV proton beam produced by the 2 MV Tandetron® accelerator ALTAIS at the PMR-LARN Laboratory (University of Namur). In order to clearly differentiate the deposited layers from the substrate, glassy carbon substrates were employed. The thickness and chemical composition of the coatings were deduced by means of the SimTarget1.0 [32] and SIMRA 6.06 [33] codes. Non-Rutherford cross-sections were computed by SigmaCalc on the IBANDL database [34] for fitting He, Si and C yields at detection angles of 165° and 170°.

2.3. Growth model and pore analysis of simulated films

The three-dimensional kinetic Monte Carlo (kMC) code NASCAM was run to simulate the growth of the films. According to the model, particles are considered to be randomly thrown towards a substrate with specific energy and incident angle distribution functions. Once they land on the film surface, different mechanisms and surface mobility processes are induced depending on the energy of the particles and the local bond structure [29]. The energy and angle distribution function of the sputtered Si atoms at the source (i.e. the magnetron head) were calculated by means of the SRIM [35] software, whereas the SIMTRA code [32] was used to simulate the transport of these sputtered particles to any location inside the deposition reactor. Collisions of sputtered Si atoms with gas atoms determine the trajectories of the first. Collisions of Si atoms with He atoms have only a subtle effect on the trajectories of Si atoms due to a low mass ratio, as confirmed by SIMTRA calculations. Therefore, in the case of the He + Ar deposition gas, only the effect of Ar was considered in the SIMTRA simulations.

The porous structure of simulated films was analyzed by considering cross-sectional slices of material. The key number, in this case, is the so-called pore throat, π_t. This quantity topologically characterizes the porous structure: two voids within the material are considered connected and, thus, to belong to the same pore if a circle of diameter π_t covers a continuous path from one to the other without intercepting any material. If such a path does not exist, both voids are considered to belong to different pores. Moreover, a void is considered occluded if it has no connectivity with the empty space above the film (see figure 3). For pore analysis the software PORESTAT developed for NASCAM simulation analysis was used (more information see [36]).

3. Results and discussion

3.1. Microstructural and chemical characterization of the coatings

The upper part in figure 4 shows the SEM cross-section views of the amorphous silicon coatings. Thickness and deposition rates have been evaluated from these micrographs and summarized in table 1. The lower part of this figure presents a closer view by means of TEM cross-section micrographs of
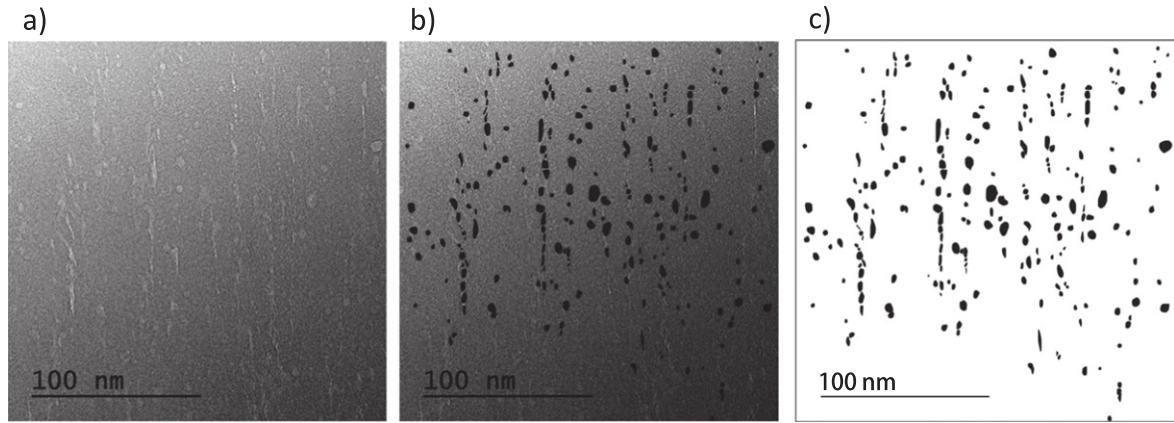
a)

b)

c)

100 nm

100 nm

100 nm

Figure 2. (a) As recorded TEM image; (b) pore identification and selection on TEM image; (c) selected pores.

One Pore

Two Independent Pores

Non-Occluded Void

π_t

π_t

π_t

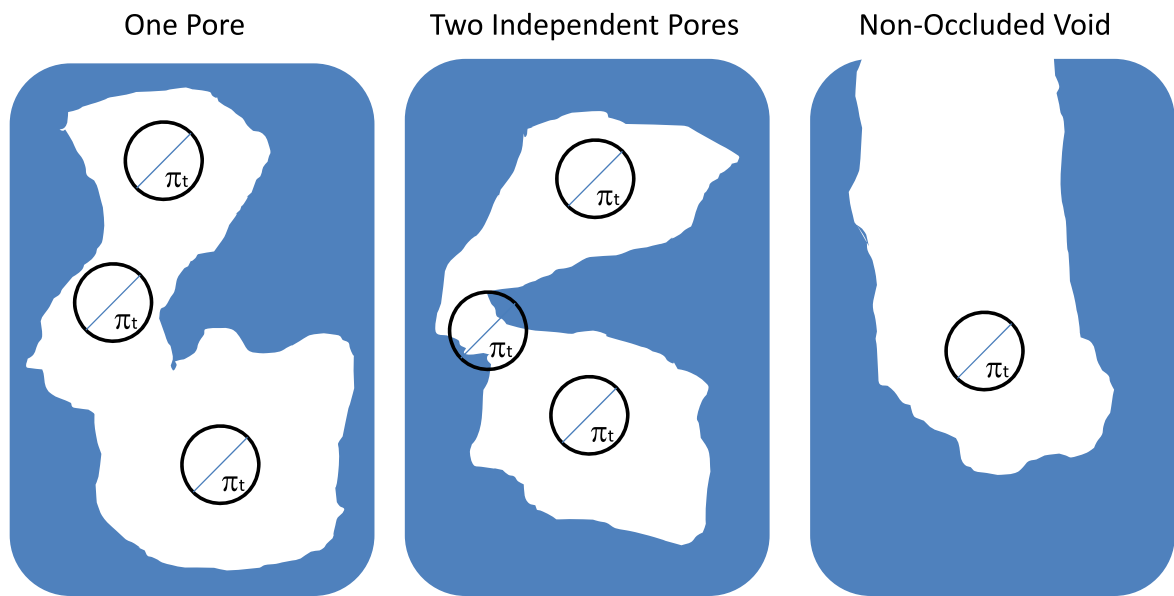π_t

π_t

π_t

π_t

Figure 3. Pore throat definition.

the selected samples and illustrates the influence of the geometry (Z1 and Z2) and the chemical nature of the processing gas (Ar and He + Ar mixture) on the films' porosity. In these images, the white contrast features correspond to the pore structures. In general, and regardless of the chemical nature of the sputter gas, films show a tilted porous structure aligned along a certain preferential direction. This behavior can be qualitatively explained by considering only the surface shadowing effects [24, 37]. In OAD, the particle flux towards the substrate is nearly unidirectional, inducing self-shadowing processes that produce tilted porous patterns and decrease the film density [24, 37]. The TEM images in figure 4 also show larger and better-defined pores for the samples grown under He + Ar mixtures. A detailed discussion on pore size distributions and shapes will follow below.

Of particular interest is the fact that a white contrast can be observed in figure 4 at the interface between substrate and coating. RBS analysis was also undertaken and whose results are shown in figure 5. Depth profiles for Si, O, He and C clearly show the substrate, coating and interlayer in between.

Table 1 presents the chemical composition of the porous coating as obtained by the RBS analysis. Films are mainly made of Si, with a considerable amount of oxygen when grown in the Z2 oblique incidence region, regardless of the processing gas used. Taking into account that both films were grown simultaneously in each region (Z1 and Z2) and, hence, exposed to the same atomic gas species during growth, this oxygen can only appear when the films are exposed to air. In this regard, films grown in the more oblique incidence region (Z2) seem to possess a more open (non-occluded) porous structure and, therefore, a larger surface area in contact with air. In addition to this main post-deposition oxidation, the interlayer observed in figure 4 on the silicon substrate prior to the coating also corresponds to a SiO_x composition as concluded from depth profiles in figure 5. In this case, the layer is most probably due to insufficient target cleaning and a native oxide layer on the silicon. In figure 6, we show EFTEM images recorded with a 4 eV window at 17 and 24 eV for the four selected samples. The plasmon losses centered at these two selected energies are characteristic of Si and SiO2,
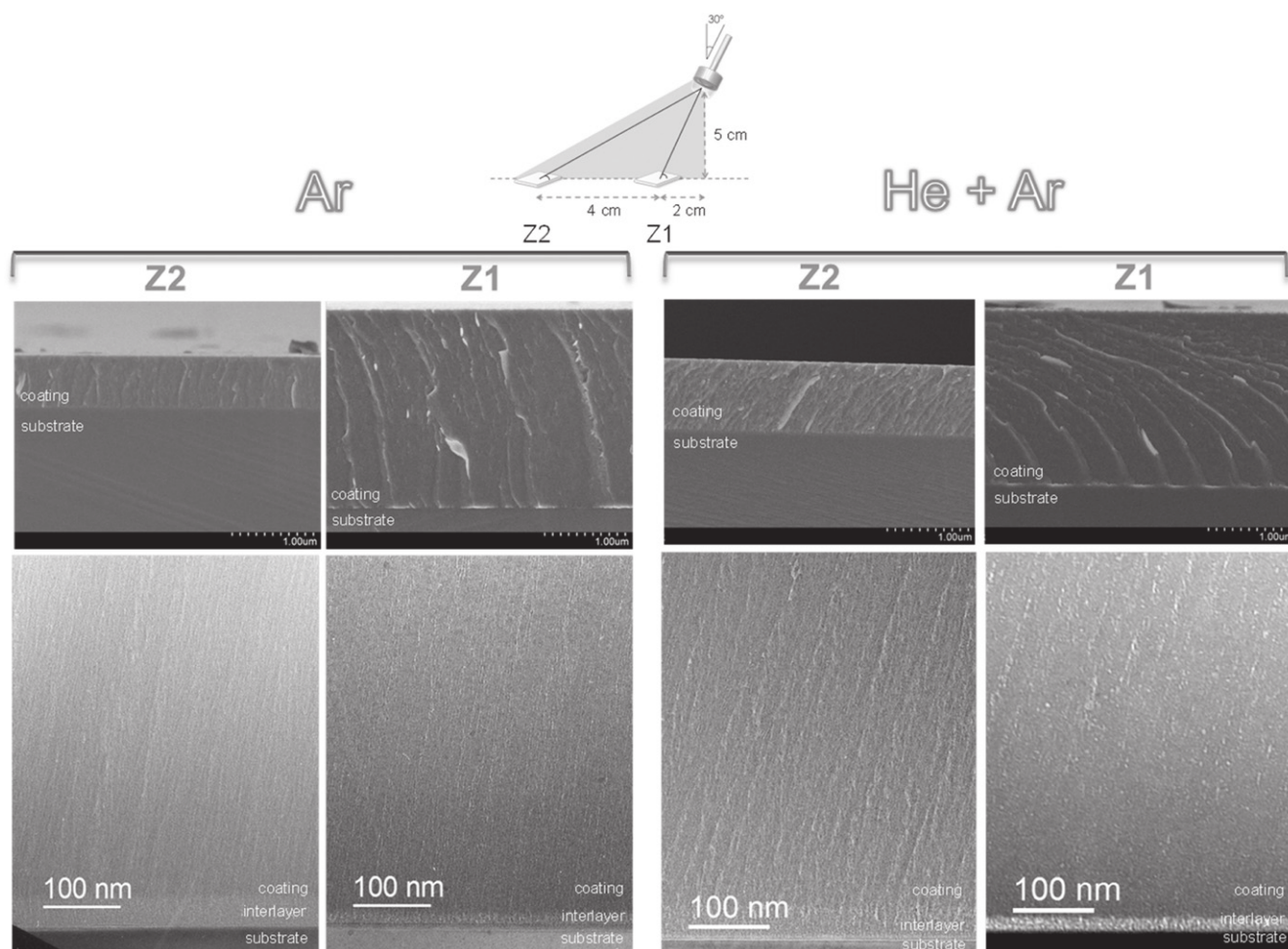
Figure 4. SEM cross-sectional views (top) and low magnification TEM cross-sections (bottom) for the four selected conditions.

Table 1. Composition of the coatings by RBS and ERDA results, density calculated from the RBS results considering only the Si atoms in the film; thickness given by RBS and SEM in cross-sectional views; deposition rate calculated from SEM results.

Dep. gas	Zone	Composition in at%				Density[a] at nm^{-3}	Thickness 10^{15} atm cm^{-2} (RBS)	Thickness nm (SEM)	Dep. Rate (nm min^{-1})
		Si	He	Ar	O				
He+Ar	1	90.3 ± 0.5	6.7 ± 0.1	1.5 ± 0.2	1.5 ± 0.2	44.1 ± 0.2	9300 ± 370	1880	37.6
	2	80.4 ± 0.4	2 ± 0.03	0.6 ± 0.1	17 ± 0.2	36.2 ± 0.2	4400 ± 180	930	18.6
Ar	1	98.9 ± 0.1	0	0.6 ± 0.1	0.5 ± 0.0	49.2 ± 0.2	9300 ± 370	2030	50.8
	2	82 ± 0.2	0	0	18 ± 0.2	39.8 ± 0.2	4400 ± 180	820	20.5

[a] Density of compact crystalline Si = 50 at nm^{-3}

respectively, and the images in figure 6 represent chemical maps of the two phases. Especially in the images at 24 eV, electron losses are a good indication of the silicon oxidation produced by exposure of the coatings to air. It is quite clear that open porosity is characteristic of films grown under a more oblique deposition (Z2). The results presented closely fit other, previously-reported data [24, 37] and are explained by taking into consideration the main shadowing effect during OAD, as will also be validated in simulations to be discussed in the final section of this paper.

The incorporation of processing gas atoms in the coatings was also measured. The low amount of Ar incorporated into the films, when Ar is the sole gas in the reactor, is also particularly relevant. Indeed, a tiny quantity (0.6%) of argon atoms can be detected only when the film is grown in Z1, whereas a negligible number (0%) is found in the more oblique incidence region Z2. This result also matches the view that the film grown in the oblique incidence region possesses a larger surface area and, hence, that desorption mechanisms are more efficient. In this regard, it is worth remarking that as the films reach temperatures of up to 130° C
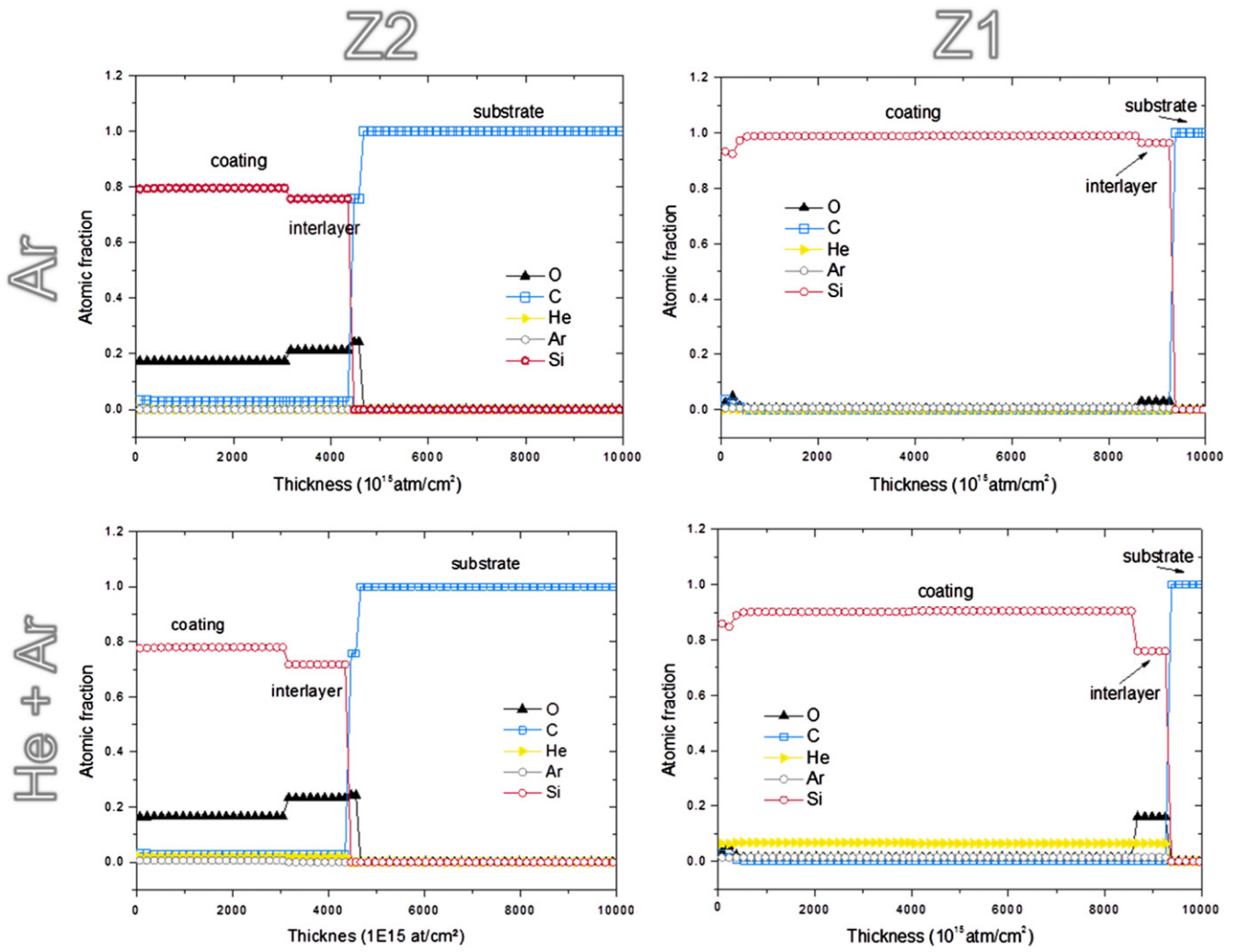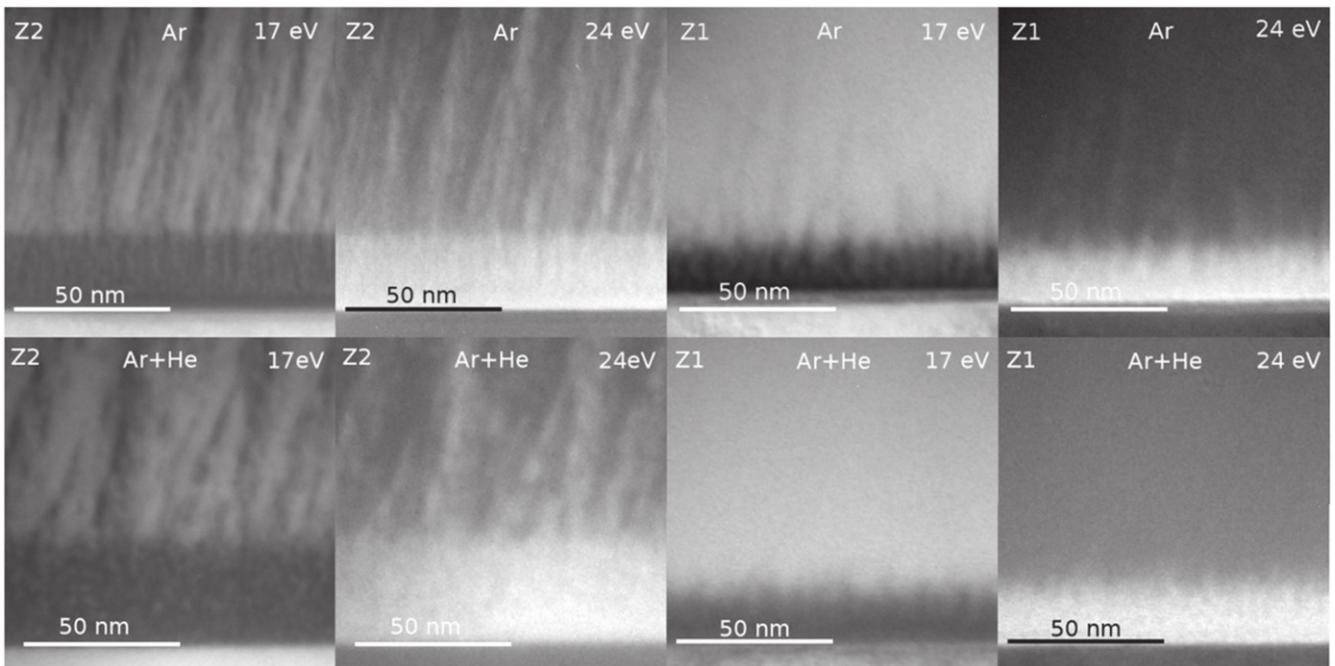
Figure 5. RBS elemental profiles.

Figure 6. EFTEM images with a 4 eV window at 17 and 24 eV, representing Si and SiO2 plasmon losses, respectively.
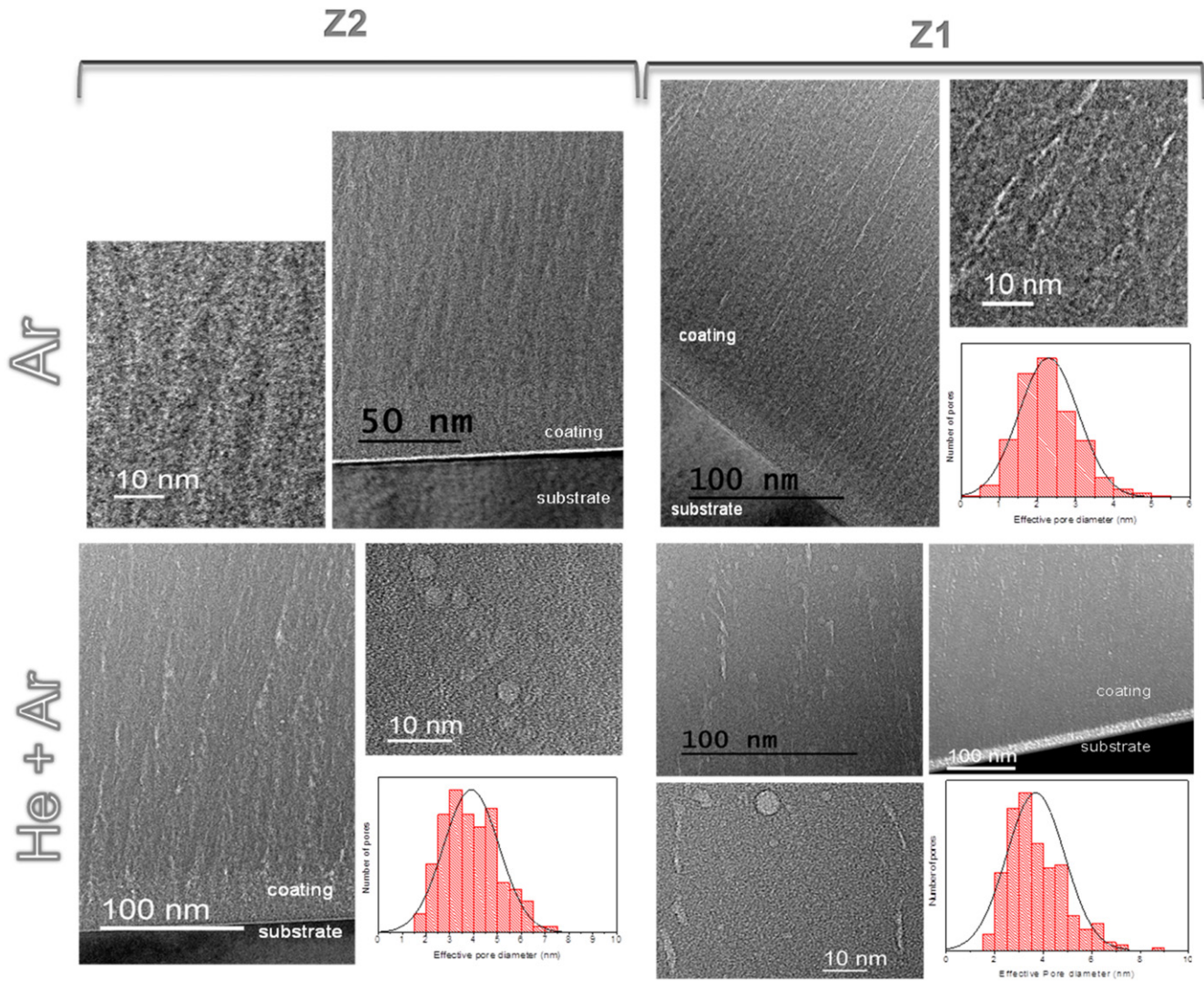
Figure 7. High magnification TEM cross-section details showing different porosity and pore size distribution.

during growth, the desorption of the gases is expected to be relevant.

According to table 1, when the He + Ar mixture was used, He and Ar atoms were found in both regions with a ratio of He to Ar of about ~4.4 (Z1) and ~3.3 (Z2). These values can be explained by considering the thermal flux of Ar and He gas atoms impinging on the films during growth, F_{Ar} and F_{He}, respectively, that read

$$F_{Ar} = \frac{1}{4} N_{Ar} \sqrt{\frac{8k_B T}{\pi M_{Ar}}} , \qquad F_{He} = \frac{1}{4} N_{He} \sqrt{\frac{8k_B T}{\pi M_{He}}} ,$$

where N is the density of each gas in the gas phase, M the atomic mass, k_B the Boltzmann constant and T the gas temperature. Therefore, the ratio between both fluxes is $F_{He}/F_{Ar} = N_{He} \sqrt{M_{Ar}} / N_{Ar} \sqrt{M_{He}}$, knowing that $N_{He}/N_{Ar} \sim 1.7/0.8 = 2.1$ yields $F_{He}/F_{Ar} \sim 6.6$. This result, together with the well-known fact that He desorbs from the material better than Ar due to its lower mass and smaller size, explain why the experimental ratio between both gases is between 3 and 4. Furthermore, the lower amount of both gases when film grows in the more oblique incidence region Z2 coincides with

the idea that it possesses a higher surface area. Thus, He and Ar atoms may desorb more easily. The nanostructural features described above can therefore be qualitatively explained by considering the thermalization degree of the sputtered particles by gas-phase collisions [26], the typical shadowing effects [24] and desorption processes during film growth.

An estimation of coating densities can be calculated from RBS results and compared with the theoretical value for Si (the density of crystalline silicon is about 50 at nm^{-3}). The density values presented in table 1 were calculated considering that only Si atoms contribute to the bulk of the coatings. The density values obtained indicate that the coatings are porous and, in general, that films deposited with He + Ar are less dense than those deposited with pure Ar. Coatings deposited in Z2 present a higher porosity in both cases.

With the aim of analyzing the pore sizes and shapes for the occluded porosity, a closer inspection was performed by higher resolution TEM cross-section analysis shown in figure 7. The figure also indicates the average pore size distribution function, as obtained through the analysis of the
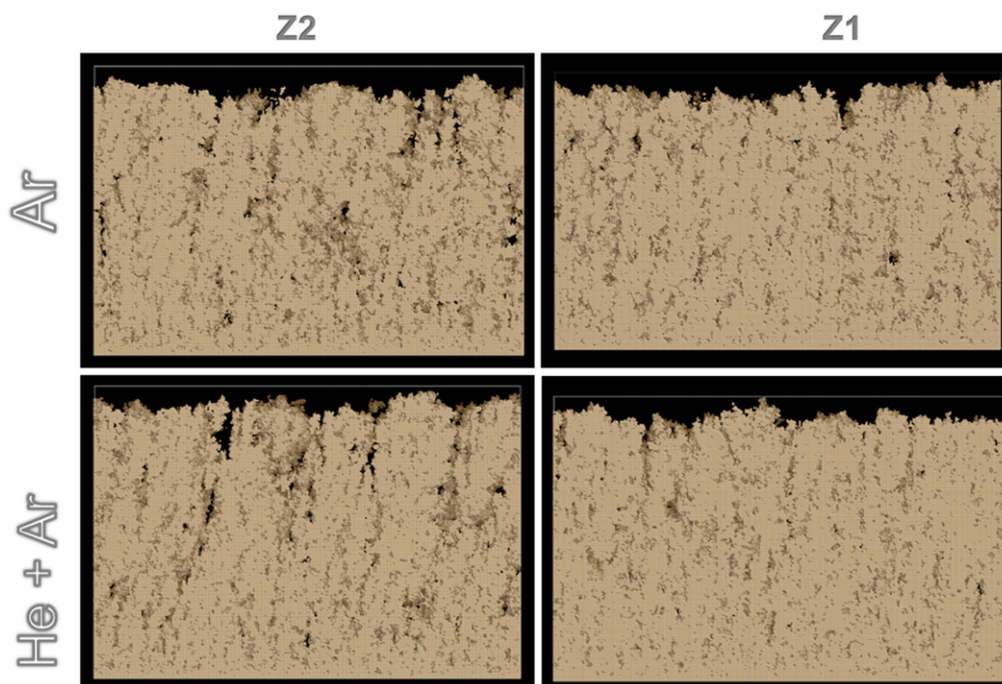
Figure 8. NASCAM simulation results for the two zones 1 (Z1) and 2 (Z2) for Ar and He + Ar working conditions with substrate dimensions of 120 nm × 30 nm and total number of deposited Si atoms of 2×10^6.

TEM micrographs following the procedure described in the experimental section. When argon only gas was employed (upper part of figure 7), it was not possible to clearly identify the small pores when going to high magnification images for the film grown in Z2. The pore size distribution function was rather arbitrary and inconclusive, so we have not included them. For the films grown in Z1 it was possible to measure numerous elongated small closed pores with sizes of around 2 nm and below which are also clearly aligned. The number of these pores decreases as larger sizes are considered. Interestingly, when the mixture He + Ar is used (figure 7, down), pore size distribution on films grown in the same Z1 region show a very small amount of pores around 2 nm and below with a higher number of bigger pores, showing a considerable amount of pores from 3 nm up to 6 nm. This result becomes even more evident in figure 7 (bottom) for the pore size distribution of the film grown in Z2 using the Ar + He mixture. Pores start at 2 nm in size and go up to 7 nm, with the majority falling around 4 nm.

Another interesting aspect concerns the shape of the pores, which can be discerned after a closer inspection of the high-resolution images in figure 7. When the films are grown using Ar, pores are elongated and the microstructure can be defined as a series of elliptical pores one after another, in some cases being difficult to determine where one pore ends and the following one begins. This scenario fits a typical OAD, where column broadening and extinction result in microstructures with high inter- and intra-columnar porosity. The coatings deposited employing the mixture of He and Ar, on the other hand, present clearer and more rounded pores, together with other pores that are elongated. Indeed, it seems that the presence of He in the deposition gas leads to rounder

pores, as shown in a previous paper [8], and has been reported for dc sputtering of metals using He and Ar mixtures [15–17].

In the following section, we describe our simulation results, taking into account only the thermalization degree of the sputtered particles by gas phase collisions and the typical shadowing effects under dc conditions. The comparison with experimental data will show that the introduction of the He gas in the plasma, as well as the geometry are crucial to enhance closed porosity formation, as we had previously proposed from purely experimental data [8].

3.2. Comparison between experiments and simulations

The results of the NASCAM simulations are presented in figure 8 for the four selected experimental conditions. The simulation size taken is 120 nm × 30 nm and the total number of effective particles amounts to 2×10^6, with a simulated film thickness of about 30 nm. The darker zones in figure 8 correspond to the porosity in the coatings, while the lighter ones correspond to the silicon matrix. In this case, the selected pore throat is $\pi_t = 0.9$ nm for a clear view. The model describes fairly well the main features of the porous tilted microstructures presented in figure 4. As expected, films grown in the more oblique Z2 position show a higher pore density. In addition, post-modeling analysis also allows for the determination of the actual film area in contact with air (i.e. non-occluded porosity) as shown in figure 9. Coinciding with previous findings [24], as well as the RBS described previously (table 1 and figure 5) and EFTEM (figure 6) analyses, the coating grown in the more oblique incidence region (Z2) shows a greater number of open voids penetrating deeper into the bulk of the film, a feature implying a larger film surface in contact with air which, in turn, coincides with the
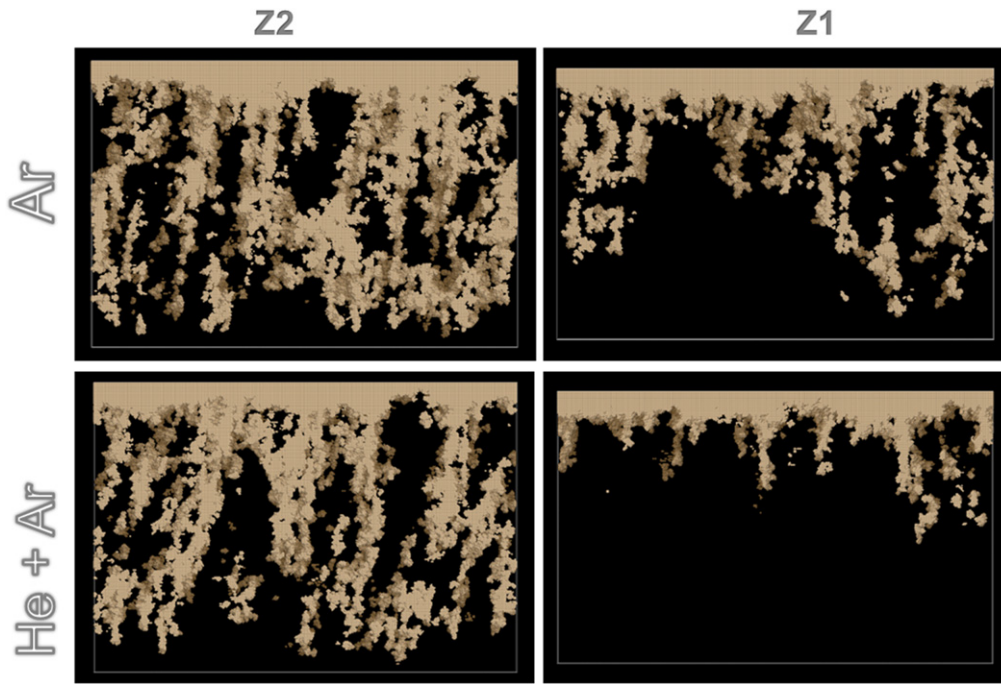
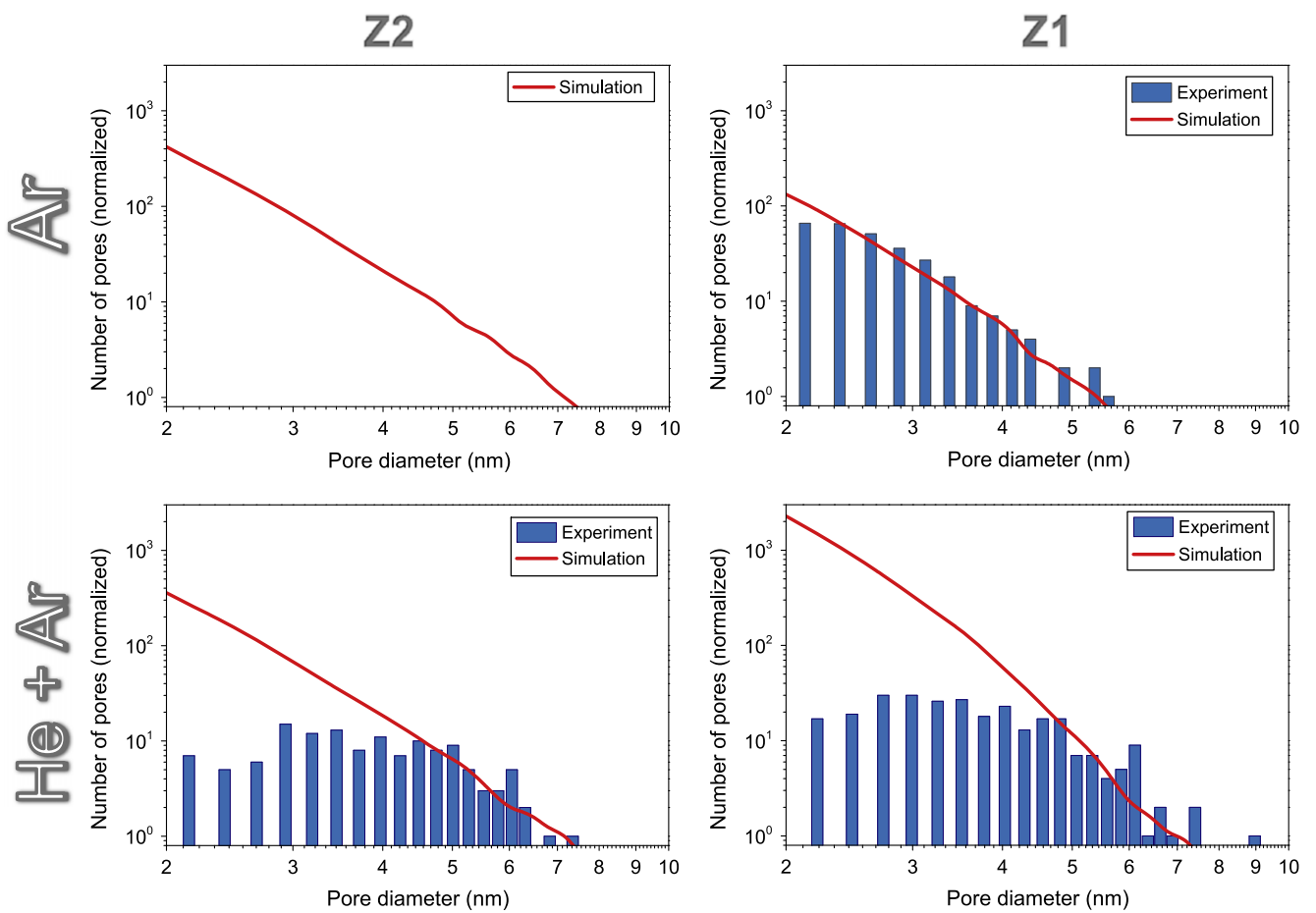**Figure 9.** Simulation results of pores connected to the surface.

Figure 10. Theoretical pore size analysis versus experimental results for positions Z1 and Z2 of (a) Ar and (b) He + Ar deposition gases.

abovementioned discussions concerning the effects of surface shadowing.

Figure 10 shows a comparative analysis of pore size measured by cross-section TEM micrographs and the results of closed porosity provided by the simulations. A pore throat of $\pi_t = 2$ nm was considered for this analysis. As, according to IUPAC, 2 nm is the critical pore size separating micropores and mesopores, our description would correspond to a pore connectivity analysis through mesopores. Experimental data is the same as that shown in figure 7, while representing the number of pores starting with an average diameter of 2 nm. The normalized number of pores represents the total number of pores as a function of the pore diameter normalized to the corresponding number of pores observed experimentally. Figure 10(a) shows the results of pore sizes for the coatings deposited in pure Ar. In the case of a film grown in Z1, the model reproduces the experimental trend and shadowing effects completely explain the different porosity, pore distribution and orientation. Figure 10(b) presents the results for the film deposited using the mixture of He and Ar. Although a certain similarity is found in the results for the medium-large size pores, the results from the TEM and simulations seem to differ for the rest of the pore diameter range. Therefore, the surface shadowing mechanism cannot satisfactorily explain the pore structure of the films whenever He is introduced in the reactor, regardless of whether the growth takes place in Z1 or Z2 position. The use of He seems somehow to introduce a new process affecting the nanostructural development of the films. In this case, it is remarkable that if surface shadowing dominated the pore formation, smaller pores would be more abundant than larger ones. This suggests that in the presence of He in the sputter gas, a new nanostructuration process governs the pore dynamics that tend to merge small pores and turn them into larger occluded ones. Interestingly, there are many studies [20, 22, 23] on the behavior of embedded He atoms that, after being implanted, stay in the metallic material and promote the migration of point defects in the network in order to form He bubbles. Remarkably, this process would explain the existence of larger pores in the higher magnification images in figure 7(b), as well as the rounder aspect of the pores. In this regard, the results presented in this paper infer that such a mechanism is present and relevant when He is employed for producing films by magnetron sputtering.

From our previously published experimental results [8], other experimental conditions, like the use of RF power, may additionally enhance the formation of closed pores under He plasma conditions. Theoretical calculations including matrix mobility and a higher potential for the He plasma will be the object of future research.

4. Conclusions

In this paper, we demonstrate that the processing gas plays a key role in the nanostructural development of the films, not only regarding the sputtering process or collisional events in the gaseous/plasma phase, but also in the dynamics of the deposited matrix atoms, in particular concerning the porous

structure of the films. For this, we have investigated the microstructural evolution and pore formation in an a-Si coating deposited by magnetron sputtering at oblique angles in low dc power conditions using Ar and He as the sputter gas. We have employed a simple Monte Carlo model (NASCAM) to explain the formation of the porous structures that only considers the surface shadowing mechanism of sputtered Si atoms. In this way, the model accurately reproduces the size, shape and orientation of the pores when Ar is employed as a processing gas. When He is introduced in the reactor, a new mechanism seems to take over, which tends to merge small pores and form large ones. This mechanism could be similar to previously reported bubble formation processes. These processes have been associated with certain mobility of point defects in the Si network due to the low solubility of He in the material.

Acknowledgments

References

[1] Becker C *et al* 2012 Large-area 2D periodic crystalline silicon nanodome arrays on nanoimprinted glass exhibiting photonic band structure effects *Nanotechnology* **23** 135302
[2] Jin H and Liu G L 2012 Fabrication and optical characterization of light trapping silicon nanopore and nanoscrew devices *Nanotechnology* **23** 125202
[3] Spinelli P, Verschuuren M A and Polman A 2012 Broadband omnidirectional antireflection coating based on subwavelength surface Mie resonators *Nat. Commun.* **3** 692
[4] Zhang K *et al* 2012 Fast flexible electronics using transferrable silicon nanomembranes *J. Phys. D: Appl. Phys.* **45** 143001
[5] Bisi O, Ossicini S and Pavesi L 2000 Porous silicon: a quantum sponge structure for silicon based optoelectronics *Surf. Sci. Rep.* **38** 1–126
[6] Korotcenkov G and Cho B K 2010 Silicon porosification: state of the art *Crit. Rev. Solid State Mater. Sci.* **35** 153–260
[7] Harraz F A *et al* 2008 Cylindrical pore arrays in silicon with intermediate nano-sizes: a template for nanofabrication and multilayer applications *Electrochim. Acta* **53** 6444–51
[8] Godinho V *et al* 2013 A new bottom-up methodology to produce silicon layers with a closed porosity nanostructure and reduced refractive index *Nanotechnology* **24** 275604
[9] Godinho V and Fernandez A 2009 Procedimiento de obtención de recubrimientos mediante pulverización catódica y recubrimiento obtenible mediante dicho procedimiento *Spanish Patent 200930085*
[10] Godinho V *et al* 2010 SiOxNy thin films with variable refraction index: microstructural, chemical and mechanical properties *Appl. Surf. Sci.* **256** 4548–53

[11] Godinho V, Rojas T C and Fernandez A 2012 Magnetron sputtered a-SiOxNy thin films: a closed porous nanostructure with controlled optical and mechanical properties *Microporous Mesoporous Mater.* **149** 142–6

[12] Álvarez R *et al* 2011 Theoretical and experimental characterization of TiO$_2$ thin films deposited at oblique angles *J. Phys. D: Appl. Phys.* **44** 385302

[13] Álvarez R *et al* 2010 Morphological evolution of pulsed laser deposited ZrO$_2$ thin films *J. Appl. Phys.* **107** 054311

[14] Vasco E, Zaldo C and Vázquez L 2001 Growth evolution of ZnO films deposited by pulsed laser ablation *J. Phys.: Condens. Matter.* **13** L663

[15] Jia J-P *et al* 2007 Preparation of Al thin films charged with helium by DC magnetron sputtering *Nucl. Instrum. Methods Phys. Res.* B **263** 446–50

[16] Shi L *et al* 2005 Helium-charged titanium films deposited by direct current magnetron sputtering *Thin Solid Films* **479** 52–8

[17] Zheng H *et al* 2005 Introduction of helium into metals by magnetron sputtering deposition method *Mater. Lett.* **59** 1071–5

[18] Zhou Y L *et al* 2011 Study of helium evolution in nanocrystalline titanium films by slow positron beam analysis *J. Phys.: Conf. Ser.* **262** 12017–20

[19] Evans J H 2002 Mechanisms of void coarsening in helium implanted silicon *Nucl. Instrum. Methods Phys. Res.* B **196** 125–34

[20] Wilson W D, Bisson C L and Baskes M I 1981 Self-trapping of helium in metals *Phys. Rev.* B **24** 5616–24

[21] Jäger W *et al* 1982 Density and pressure of helium in small bubbles in metals *J. Nucl. Mater.* **111–112** 674–80

[22] Morishita K 2007 Nucleation path of helium bubbles in metals during irradiation *Phil. Mag.* **87** 1139–58

[23] Pizzagalli L, David M L and Bertolus M 2013 Molecular dynamics simulation of the initial stages of He bubbles formation in silicon *Modelling Simul. Mater. Sci. Eng.* **21** 065002

[24] Alvarez R *et al* 2013 Growth regimes of porous gold thin films deposited by magnetron sputtering at oblique incidence: from compact to columnar microstructures *Nanotechnology* **24** 045604

[25] Alvarez R *et al* 2010 On the microstructure of thin films grown by an isotropically directed deposition flux *J. Appl. Phys.* **108** 064316

[26] Garcia-Martin J M *et al* 2010 Tilt angle control of nanocolumns grown by glancing angle sputtering at variable argon pressures *Appl. Phys. Lett.* **97** 173103

[27] Thornton J A 1977 High rate thick film growth *Annu. Rev. Mater. Sci.* **7** 239–60

[28] Welzel T and Ellmer K 2013 Comparison of ion energies and fluxes at the substrate during magnetron sputtering of ZnO : Al for DC and rf discharges *J. Phys. D: Appl. Phys.* **46** 315202

[29] Lucas S and Moskovkin P 2010 Simulation at high temperature of atomic deposition, islands coalescence, Ostwald and inverse Ostwald ripening with a general simple kinetic Monte Carlo code *Thin Solid Films* **518** 5355–61

[30] NASCAM. http://www.unamur.be/sciences/physique/pmr/telechargement/logiciels/nascam

[31] Rasband W S ImageJ, U.S.N.I.o.H., Bethesda, Maryland, USA, imagej.nih.gov/ij/, 1997–2012

[32] Aeken K V SIMTRA www.draft.ugent.be/

[33] Mayer M 1999 SIMNRA, a simulation program for the analysis of NRA, RBS and ERDA *AIP Conf. Proc.* **475** 541–4

[34] Gurbich A F 2010 Evaluated differential cross-sections for IBA *Nucl. Instrum. Methods Phys. Res.* B **268** 1703–10

[35] Ziegler J F, Ziegler M D and Biersack J P 2010 SRIM—The stopping and range of ions in matter (2010) *Nucl. Instrum. Methods Phys. Res.* B **268** 1818–23

[36] PORESTAT. Available from: http://nanoscops.icmse.csic.es/software/porestat/

[37] Jensen M O and Brett M J 2005 Porosity engineering in glancing angle deposition thin films *Appl. Phys.* A **80** 763–8